

Chapter 6

Raman Optical System

6.1 Chapter Outline

This chapter presents in detail the optical system used to produce a large collimated beam for driving Raman transitions. It begins with a motivation of the need to minimise intensity gradients and wavefront distortions in Section 6.2. This is followed by a description of the components that form the collimator in Section 6.3. Section 6.4 presents an overview of the retro-reflection assembly.

6.2 Requirements

This section outlines the optical characteristics of the light which affect the sensitivity of the atom interferometer. These are discussed in the context of this experiment, where gravity induces transverse motion across the light. The light beams that drive the Raman transition have a intensity profile that varies radially, e.g. along the axis parallel to gravity. The motion of the atoms through a gradient of intensity leads to

a variation in the Rabi frequency that reduces the interferometer fringe contrast and decreases acceleration sensitivity [57]. This places requirements on the beam waist size, which are discussed in Section 6.2.1.

The atom interferometer senses acceleration through the second derivative of the phase of the beat note between the two counter-propagating light fields that drive the Raman transition. Any such phase derivative that does not result from the acceleration of the atoms along the Raman axis is a source of error. One such source is distortion of the Raman beams wavefronts, which can arise from transmission through rough optical elements. In fact, the typical flatness of optical viewports is greater than desired for making a sensitive accelerometer. To avoid the need for optical viewports, the Raman optical system, described in Section 6.3, was mounted inside the chamber and built using optical elements that were manufactured to far better surface qualities than conventional optics. The effect of wavefront distortions as a source of phase noise is discussed in Section 6.2.2.

6.2.1 Gradients of Intensity

The effects of a gradient of intensity on the fringe contrast can be shown by considering an ensemble of atoms with a Gaussian distribution of position. Neglecting the effect of the ensemble's velocity distribution on the Raman detuning, the Rabi frequency Ω varies only as a function of the radial displacement ρ from the optic axis. The fringe contrast is then a convolution of the contrast for a single atom with the atomic density distribution

$$\mathcal{C} = \int_0^\infty \frac{\rho}{\sigma_c^2} e^{-\rho^2/(2\sigma_c^2)} \mathcal{C}(\Omega(\rho - \rho_1), \Omega(\rho - \rho_2), \Omega(\rho - \rho_3)) \, d\rho \quad (6.1)$$

where σ_c is the rms radius of the atom cloud projected along any one Cartesian axis. The fringe contrast for a single atom, denoted by c , is defined in equation (2.27). The arguments refer to the Rabi frequency during each pulse. The duration of each pulse is chosen such that an atom at the centre-of-mass radius ρ_i has a $\pi/2$ or π rotation. It is assumed that the two light beams which drive the Raman transition have the same waist size and Rabi frequency, determined by the product of the electric fields (see equation (2.15)). Therefore, the position-dependent Rabi frequency is

$$\Omega(r) = \Omega_0 e^{-2\rho^2/w^2} \quad (6.2)$$

where Ω_0 is the Rabi frequency along the optic axis and w is the waist size – the distance at which the electric field falls to $1/e$ of its peak value.

Figure 6.1 shows the fringe contrast as a function as beam waist for an atom cloud of rms radius $\sigma_c = 5$ mm and a time between interferometer pulses of $T = 25$ ms for three cases. The blue curve shows the contrast when the atom cloud is initially at the centre of the laser and falls from rest under gravity so that centre-of-mass coordinates are $(0, -\frac{1}{2}gT^2, -2gT^2)$ respectively. The orange curve includes the vertical velocity of $u = 25$ cm s⁻¹ that the atoms are launched with by the molasses. Finally, the green curve displaces the starting position of the atom cloud to an initial position $\rho_0 = \frac{uT}{2} - \frac{gT^2}{4}$, so that each pulse is displaced by the same amount from the centre of the beam and the cloud sees the same intensity gradient. For small beam waists, the intensity gradient across the cloud significantly reduces the fringe contrast, particularly when the atoms are not launched. A beam waist much greater than the width of the cloud is necessary to achieve a large contrast.

The velocity distribution of the atoms introduces a detuning to each interferometer pulse due to the Doppler shift, as well as modifying the spatial distribution due to thermal expansion. Figure 6.2 shows the fringe contrast when including the one-

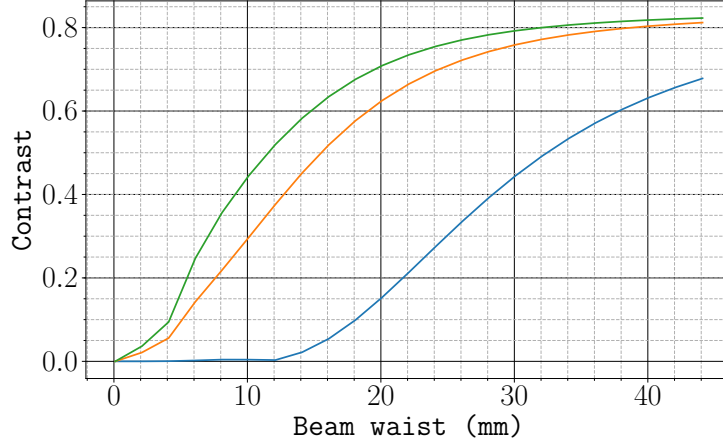


Figure 6.1: Simulated fringe contrast as a function of waist size w for an atom cloud falling under gravity. This model assumes a Gaussian distributed atomic density with a rms radius $\sigma_c = 5$ mm and a time between interferometer pulses of $T = 25$ ms. The blue curve shows the contrast when the atoms fall from rest under gravity. The orange curve includes the vertical launch velocity provided during the molasses phase. In the green curve, the atoms are displaced from the centre such that each pulse has the same intensity gradient (see text).

dimensional velocity distribution of an atom ensemble with a temperature of $5 \mu\text{K}$. The most significant difference is for small beam waists in the case of no initial launch velocity, where the contrast is now less suppressed. Aside from this, the fringe contrast is not hugely affected by the velocity distribution of the atoms.

6.2.2 Wavefront Distortions

Systematic Effects

The field that drives the Raman transition comes from the superposition of the two counter-propagating Raman beams. Ideally, these are Gaussian beams and with a beam waist of 35 mm, the Rayleigh length $z_R \approx 5$ km means that when collimated, the two beams have an almost identical radius of curvature. In this case, the effective field will have a planar wavefront. However, if the beams are not collimated they will have

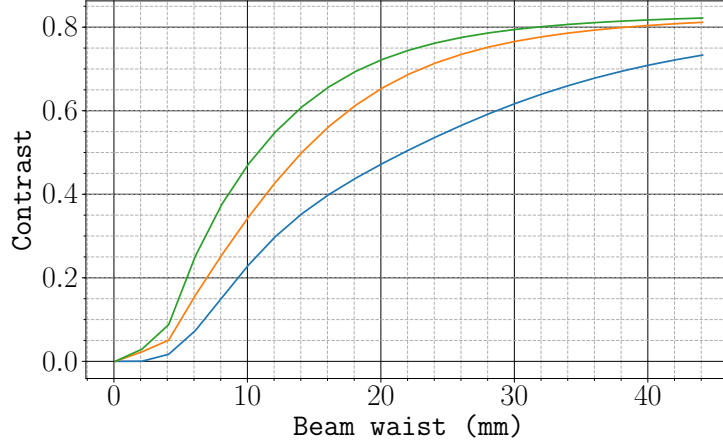


Figure 6.2: Simulated fringe contrast as a function of waist size w , including the effects of a velocity distribution along the Raman beam corresponding to a temperature of $5 \mu\text{K}$. The other parameters are the same as those used in Figure 6.1.

different radii of curvature and their superposition will therefore have a parabolic wavefront. Each Raman pulse will impress a different phase to an atom falling under gravity, leading to a component of the interferometer phase that does not cancel out. If the incoming beam has a spherical wavefront with a radius of curvature $R_1 = z_0 + \frac{z_R}{z_0}$ and a divergence angle θ , the reflected beam, which has propagated a further distance of $2L$ has a radius of curvature $R_2 = R_1 + 2\theta L$. These have respective phases of ikz^2/R_1^2 and $-ikz^2/R_2^2$, where $k = 2\pi/(780 \text{ nm})$. For an atom falling under gravity located between the output of the collimator and the retro-reflecting mirror such that $z_0 = L = 7.5 \text{ cm}$, a divergence angle of $\theta = 1 \text{ mrad}$ contributes $8 \times 10^{-12} \text{ rad}$ to the interferometer phase for a pulse separation of $T = 25 \text{ ms}$. Provided that the beams are reasonably well-collimated, this effect can be largely neglected as it is unlikely to be a dominant source of error.

A more significant contribution arises if there is a tilt of the retro-reflecting mirror. If the reflected beam is not counter-propagating, then to first order this results in a linear gradient in the Raman phase difference $\phi \rightarrow \phi + \alpha z$. After falling under gravity, this gives a false acceleration of $a_{\text{false}} = -\alpha g/k_{\text{eff}}$. A false acceleration of $a_{\text{false}} = 100 \text{ ng}$

results from a Raman phase gradient of $\alpha = 1.6 \text{ rad m}^{-1}$ and corresponds to a tilt of the retro-reflecting mirror of $0.1 \text{ } \mu\text{rad}$. Section 6.4.1 describes a method used to ensure good alignment of the mirror is discussed later, which renders this error negligible.

Random Sources of Phase

The propagation through rough optical elements distorts the wavefronts and introduce a spatially varying component of the Raman phase that is independent of acceleration. If this phase is common to both beams then it does not affect the atomic phase induced by the Raman transition. It is necessary only to consider the difference in the phase of the two light fields. If an atom's trajectory is parallel with the Raman axis, then this phase difference is the same at each laser pulse and makes no contribution to the interferometer phase for that atom. On the other hand, the Raman phase difference can change if the atom moves transverse to the Raman axis and that contributes to the interferometer phase of the atom. If that is the same for all atoms in the cloud then we are once again describing the systematic error discussed immediately above. If it differs for different atoms, then there is a loss of fringe visibility that we estimate now.

For simplicity, let us assume that the interferometer phase has a Gaussian distribution over the cloud with a standard deviation of σ_Φ . Denoting the random interferometer phase as $\delta\phi$, the fringe pattern for a single atom is

$$F = \cos(\phi + \delta\phi)^2 \quad (6.3)$$

Following from this, the fringe pattern averaged over the cloud is

$$\langle F \rangle = \frac{1}{\sqrt{2\pi}\sigma_\Phi} \int \cos(\phi + \delta\phi)^2 e^{-\delta\phi^2/2\sigma_\Phi^2} d\delta\phi \quad (6.4)$$

$$= \frac{1}{2}(1 + e^{-2\sigma_\Phi^2} \cos(2\phi)) \quad (6.5)$$

This give a fringe contrast of

$$\mathcal{C} = e^{-2\sigma_\Phi^2} \quad (6.6)$$

Figure 6.3 shows the fringe contrast as a function of this random phase. Given the high quality of the optical elements (see Section 6.3), it seems unlikely that the wavefront will wobble by more than $\lambda/50$ over a transverse region of 5 mm. I therefore expect that σ_Φ will not exceed 100 mrad and hence the loss of contrast from this mechanism will not be large. However, one can see that it is important to use optical components of high quality and that the standard $\lambda/20$ is likely to produce fringes of low contrast.

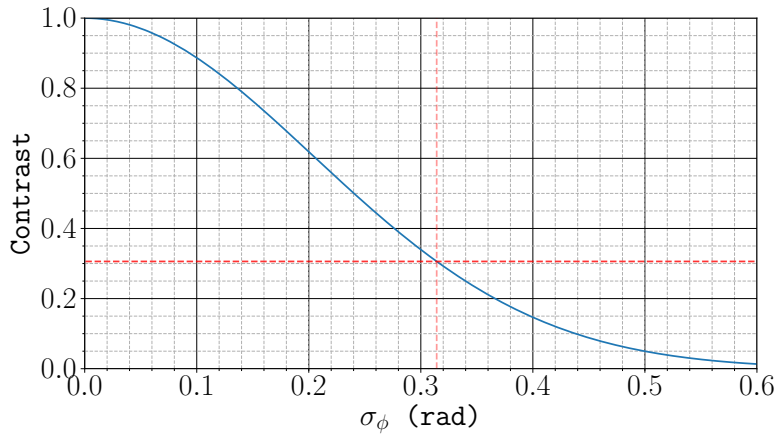


Figure 6.3: Expected contrast as a function of random phase contributions. This assumes that the phase imprinted on an atom during each interferometer pulse has an additional random component that is Gaussian distributed around 0 with a standard deviation of σ_ϕ . This random phase is also uncorrelated between each pulse so that the total can be obtained using Gaussian propagation of error. The dashed lines indicate the contrast for an rms phase uncertainty of $\lambda/20$.

6.3 Raman Optics

The optical system used to produce the beams for driving Raman transitions, will be referred to as the Raman Optics. For the reasons described in the previous section, this was designed to have good control over the flatness and orientation of the phase fronts of the Raman beams. Principally, the entire optical system was mounted inside the optical chamber so that the Raman light does not pass through any optical viewports before interacting with the atoms. This avoids the phase and polarisation distortions that are typically introduced by passing light through a vacuum window.

6.3.1 Component Overview

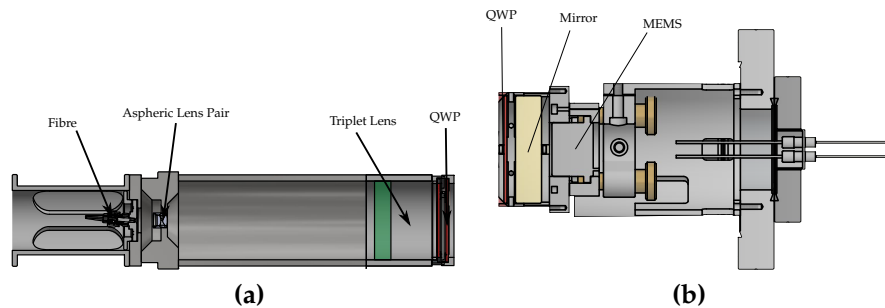


Figure 6.4: Diagrams of the components used in the Raman optical assemblies. **(a)** shows the collimator setup. Light is coupled into the chamber using a UHV fibre feedthrough. A pair of aspheric lenses is used to increase the divergence angle of the fibre output, before the light is collimated by a triplet lens. Finally, a quarter-wave plate is aligned so that it circularly polarises both collimated light fields. **(b)** illustrates the other half of the setup, which is used to retro-reflect the light. A second quarter-wave plate is used so that the reflected beams have the reversed circular polarisation. A MEMS accelerometer is mounted on the back of the mirror to measure vibrations. These components are all mounted on a piezo-controlled mirror mount whose tilt can be controlled from outside the vacuum chamber.

Figure 6.4a presents a diagram of the components used to send Raman light into the chamber and produce a collimated beam in the centre of the chamber. The light is coupled into the chamber using a UHV compatible Polarisation-Maintaining (PM)

fibre, manufactured by Diamond photonics. This is a kapton-coated PM-780 HP fibre that is bonded on one end to a DN16 flange using an epoxy resin. The external side of this flange has an FC/APC connector for coupling light from another fibre. Inside the chamber, the output of the fibre plugs into to an FC/APC fibre plate. This is clamped between a piece which bolts onto the inside of a DN63 flange and another stainless steel plate which bolts onto the rest of the optics assembly. Fine adjustment of the position of the fibre along the optic axis is achieved using shim plates with a thickness ranging from 200–300 μm . The fibre plate is free to rotate so that the orientation of the fibre with respect to a Quarter-wave Plate (**QWP**) at the output of the collimator. This **QWP** is manufactured by Light Machinery, and is described further in Section 6.4. When the fibre is correctly orientated (e.g. when the slow axis of the fibre is at 45° to the slow axis of the waveplate), the two Raman light fields are orthogonally circularly polarised.

The original design for the optical system consisted of a triplet lens, as a system of three lenses is capable of correcting for the five types of Seidel aberrations that distort rays of monochromatic light. This was designed and manufactured by IC Optical Systems to deliver a wavefront quality of $\lambda/100$. Another specification for this lens system was that it had to produce a collimated beam with a waist size of around 35 mm so that the visibility of the interferometer fringes would not be limited by the effects of intensity gradients across the atoms. Unfortunately, the triplet was designed with an incorrect Numerical Aperture (**NA**). With a focal length of 123.4 mm and a diameter of 50 mm, the triplet lens has a **NA** of 0.194. However, the nominal **NA** for PM780-HP fibre used in the UHV compatible **PM** fibre is 0.12. Consequently, the light from this fibre did not fill the **NA** of the triplet lens and produced a beam with a waist of 13 mm. To address this issue, a pair of aspheric lenses was included to increase the divergence angle of light from the fibre. These are manufactured by Thorlabs and have

a focal length of 4.51 mm (352230-B) and 15.29 mm (352260-B), respectively, to give a magnification of 3.39.

6.3.2 Alignment and Collimation

As one of the main motivations for mounting the Raman optics inside the vacuum chamber was to reduce the effects of wavefront distortions, it is worth highlighting how inaccurate alignment of the optics can lead to aberrations. As previously discussed in Section 6.2.2, distortions of the wavefront can produce a false acceleration and possible loss of interferometer fringe visibility. Here, the same figures of merit as before are used to consider what misalignment is acceptable to ensure that the phase of the Raman wavefront deviates by less than $\lambda/100$ after a transverse distance of 12.5 mm (that being the distance fallen from rest after 50 ms).

Taking the fibre as a point source, misalignment can occur if it is displaced from the front focal point of the optical system either along or transversely to the optic axis. If it is transversely displaced, this manifests as an angular displacement of the collimated light after the triplet lens.

Although we do not expect to have any significant transverse misalignment of the fibre, there could be an axial one. In that case, the output beam will not be collimated. This leads to a systematic error, already discussed in Section 6.2.2, where transverse motion of the atoms produces an interferometer phase that is misinterpreted as an acceleration along the optic axis. incoming ones. The effect of this longitudinal displacement on the Raman wavefront is shown in Figure 6.5b. Further from the optic axis the deviation in the phase of the light is greater, giving a quadratic distortion which is characteristic of a defocus. Comparing the wavefront distortion in this case, a requirement on the longitudinal misalignment of < 0.6 mm is needed for the previously specified flatness.

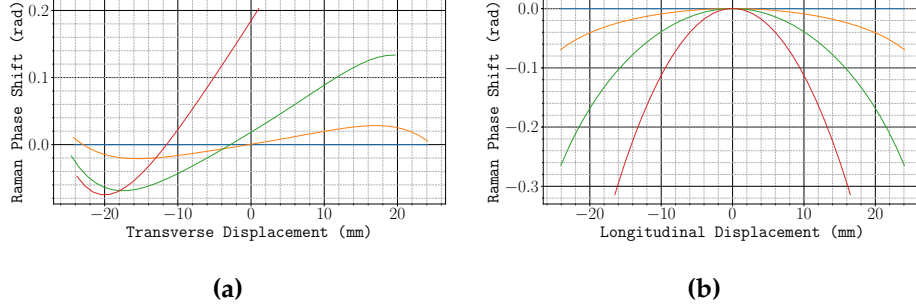


Figure 6.5: Simulated wavefront distortion for longitudinal and transverse fibre misalignment. Rays from a point source with a divergence angle corresponding to a NA of 0.12 are propagated through the Raman optical system. Rays corresponding to the reflected beam are propagated further with the assumption that the mirror is perpendicular to the optic axis. The first set of rays propagates 43 mm and the second propagates 129 mm. The wavefront for each beam is calculated by taking the slope of each ray and subtracting from the slope of the central ray. The wavefront of the effective field that drives the Raman transition is the difference of these two wavefronts. (a) shows the distortion of the wavefront for a transverse misalignment of the fibre for a displacement of 0 mm (blue), 0.5 mm (orange) 1 mm (green) and 1.5 mm (red) from the front focal point. (b) shows the wavefront for longitudinal displacements of 0 mm (blue), 0.3 mm (orange) 0.6 mm (green) and 1 mm (red).

6.3.3 Measuring the Beam Width

To measure the waist of the beam, its reflection from a flat surface was imaged using a CCD camera. The radius of the triplet lens is smaller than the beam waist, so the beam is apertured by this lens. To take account of this aperture, the beam waist was estimated using a Taylor expansion of a Gaussian to second order:

$$\begin{aligned}
 I(x) &= A e^{-\frac{(x-x_0)^2}{2w^2}} \\
 &\approx A - \frac{2Ax_0^2}{w^2} + \frac{4Ax_0}{w^2} - \frac{2Ax^2}{w^2} + \mathcal{O}(x^3)
 \end{aligned} \tag{6.7}$$

A typical intensity profile along the horizontal and vertical camera axes is shown in Figure 6.6b. A threshold intensity value excludes contributions from pixels outside of the spatial extent of the beam. The waist was estimated using a linear least-squares

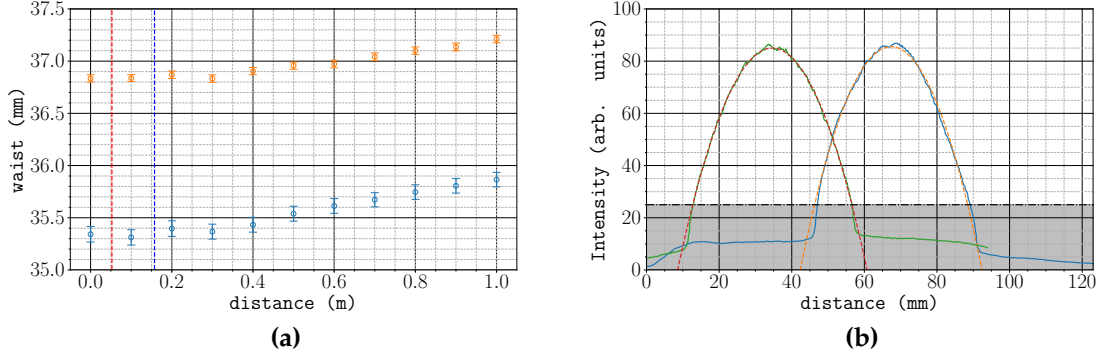


Figure 6.6: Raman beam waist measured over a distance of 1 m, shown in **(a)**. The waist along the horizontal and vertical axes are indicated in blue and orange respectively. The dashed lines indicate the approximate propagation distance of each beam at the position of the atoms. **(b)** shows the intensity profile along each axis, with the fitted parabola. The dot-dashed line is a threshold intensity value, which excludes pixels from outside the spatial extent of the beam.

fit of the intensity profile to a second-order polynomial $c_0 + c_1x + c_2x^2$, where

$$w = \left| \frac{\sqrt{c_1^2 - 4c_0c_2}}{\sqrt{2}c_2} \right| \quad (6.8)$$

A plot of the estimated beam waist over a propagation distance of 1 m is shown in Figure 6.6a. Inside the chamber each Raman beam propagates 5.25 cm and 15.75 cm, where the beam is well collimated. Along the vertical axis, the beam has a waist of around 36.9 mm. The horizontal waist is smaller because the camera was horizontally tilted from the beam's optic axis. The projection of the beam onto this axis is consistent with a horizontal tilt of 16° .

6.4 Retro-Reflection Assembly

The Raman transitions used in the interferometer are driven by counter-propagating light fields to give a large momentum transfer of $2\hbar k$ to the atoms. The two beams

enter from the same fibre input, so a mirror is used to retro-reflect them. The retro-reflection assembly includes a **QWP** to ensure that the reflected beams have the same polarisation handedness as their circularly polarised incoming counterpart.

The mirror is also manufactured by Light Machinery, and the **QWP** is made to the same specifications as the one that circularly polarises the incoming beams. During the manufacturing process, the waveplates and mirror were polished to reduce irregularities in the thickness of each **QWP** and the surface of the mirror. Figure 6.7 shows the variation in the thickness of the waveplate in front of the triplet lens, measured by Light Machinery using a white light interferometer. This has a standard deviation of 4.62 nm and corresponds a standard deviation of the optical path length of $8.6 \times 10^{-3} \lambda$. The **QWP** and mirror are fixed onto the front plate of a UHV compatible MDI-HS

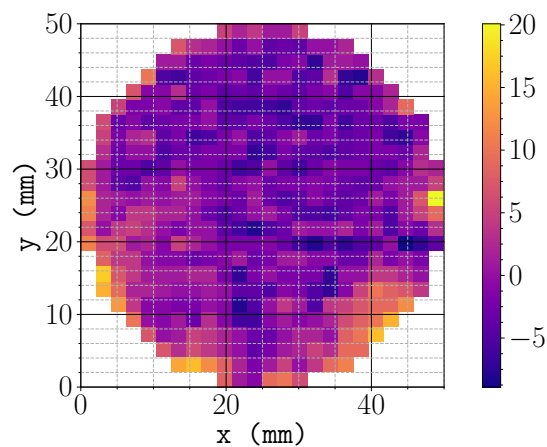


Figure 6.7: Thickness of the first **QWP**, measured by a white light interferometer. The value is given in nm as a difference from the mean thickness. The standard deviation of this thickness is 4.62 nm and a peak-to-valley (PV) of need number here. Equivalent surface data for the other **QWP** and mirror were not provided by Light Machinery, but had a PV thickness variation of 19 nm and 9 nm respectively.

mirror mount, manufactured by Radiant dye. The horizontal and vertical tilt of the mirror can be adjusted using two thumbscrew actuators which cause the front plate to pivot around a ball bearing. This mount is designed for high stability, but of course the alignment will still drift over time. To avoid the need to periodically open the chamber

to realign the mirror, a piezo-electric stack is placed between each actuator and the front plate so that the tilt of the mirror can be adjusted externally. Each piezo-stack is connected to a high-voltage feedthrough, so that their length (and hence mirror tilt) can be finely adjusted by controlling the voltage applied across them. A control voltage ranging between 0–10 V is amplified by a controller to give an applied voltage across the piezo stack between -10–150 V. This corresponds to a travel range of 23 μm .

To understand the effect of misalignment, it is instructive to consider its effect on the effective wavevector \mathbf{k}_{eff} . If the mirror is misaligned from the incoming beam's wavevector by an angle θ , the two counter-propagating fields that drive Raman transitions have wavevectors $k_1 (1, 0)$ and $k_2 (\cos(\theta), \sin(\theta))$. $\mathbf{k}_{\text{eff}} = \mathbf{k}_1 - \mathbf{k}_2 \cos(2\theta)$. Fortunately, for small angular displacements, i.e. < 1 mrad, this does not greatly reduce the sensitivity to accelerations. In short, this means that \mathbf{k}_{eff} will have a spatially varying direction. Since an atom interacting via a Raman transition picks up a phase $\phi = \mathbf{k}_{\text{eff}} \cdot \mathbf{x}$, atoms travelling along different trajectories will accumulate different phases due to the spatial variation of \mathbf{k}_{eff} . Across the atom ensemble, this leads to a dephasing and consequently, a loss of interferometer fringe visibility [59]

6.4.1 In-Situ Alignment and Optimisation

After mounting the Raman optical system inside the chamber, the mirror had to be aligned to retro-reflect the light. When the mirror is close to perpendicular to the light's wavevector, some of the power in the reflected beam couples back into the fibre. In principle, this power is maximised when the mirror is exactly perpendicular so maximising this power is a useful technique to align the mirror. A 99:1 fibre splitter was used to couple light into the chamber, which provided a means to measure the back-reflected power without needing any free-space optics. This was set up so that 99% of the incoming light entered the chamber, with the other 1% coupled into the

corresponding output port. Due to the fact that a beam-splitter acts reversibly, 1% of the back-reflected light which couples into vacuum fibre exits the fibre-splitter on the other input port. Therefore, the power at this output was used to indirectly measure the alignment of the mirror.

The travel range of the piezo stacks does not cover the full motional range of the mirror mount. It was initially coarsely aligned using the thumbscrew actuators. Once installed, the lack of direct access to optical system meant that conventional methods to coarsely align the mirror, such as observing the location of the reflected beam's focus, were not feasible. Rather than carry out the somewhat tedious job of systematically adjusting each thumbscrew until the mirror was aligned, an automatic routine was devised to do this. This was carried out using a pair of bipolar stepper motors that each rotated a ball driver inserted into the head of each thumbscrew. The revolution of these motors was controlled using an Arduino microcontroller, which communicated to the computer using a serial interface. The motors rotated by $0.9^\circ/\text{step}$, which corresponds to a tilt of the mirror by $18.1 \mu\text{rad}$. This is smaller than the 0.67 mrad angular displacement that the piezo stack could provide, but the slow execution speed of the motor control meant that it was more practical to use a combination of the motors and piezos to systematically scan through the tilt of the mirror mount.

Using this method, the mirror mount was aligned so that the maximum of the back-reflected power was reachable with the piezo stacks. Of course, it was foreseeable that the mirror would need to be periodically realigned, which would require another systematic iteration through the voltages applied to each piezo stack. Given that this search was quite time consuming, it was not a practical way to maintain alignment. To improve upon this, an optimisation method using the Nelder-Mead simplex algorithm [60] was implemented. This method is suitable for optimising multidimensional

functions and has been used to demonstrate the automatic alignment of a fibre with up to 6 degrees of freedom [61].

The Nelder-Mead algorithm aims to optimise the value of an objective function (in this instance, the optical power measured as a voltage by a photodiode) by sampling the function at various locations. For n parameters, a set of $n - 1$ points distributed randomly across the parameter space are chosen as the initial simplex. These are sorted in decreasing order of the value of the objective function and the algorithm proceeds by performing geometric transformations on this simplex, by sequentially reflecting, expanding and contracting this simplex. Each step starts with a reflection about the line between the two greatest values. The coordinates of the simplex are updated if the function has a greater value at the location given by one of these transformations, until the algorithm converges on a maximum value. As with many optimisation algorithms, the Nelder-Mead method has the potential to converge on a local optimum, but this is alleviated by expanding the simplex to look for more optimal values. The termination of the algorithm was decided by using the standard deviation of the last 5 values. Empirically, it was found that terminating when the standard deviation was less than $10\text{ }\mu\text{V}$ resulted in stable performance of the algorithm, even when the signal-to-noise ratio of the measured voltage was poor. An example of this algorithm aligning the mirror mount is presented in Figure 6.8. To verify that the converged value was optimal, a systematic scan of the piezo stack control voltages in the region around this value was also carried out. In this case, the algorithm converged on a local maximum, but one that greatly enhanced the coupling efficiency of the reflected light back into the fibre. The difference in the piezo control voltages from their optimal values corresponds to a tilt of the mirror mount along the horizontal and vertical axis of less than $13\text{ }\mu\text{rad}$.

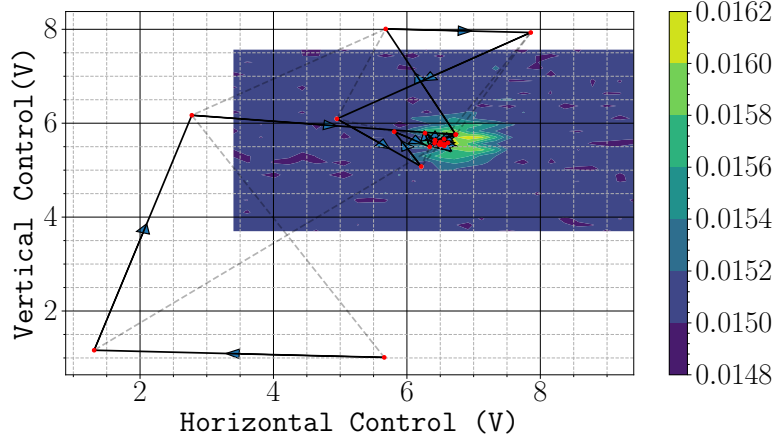


Figure 6.8: Automatic mirror alignment using the Nelder-Mead simplex algorithm. A sequence of geometric transformations on the initial simplex are used to converge on the optimum point, where the back-reflected power is maximised. The shaded lines indicate the simplex bounded by the three co-ordinates at each iteration. A raster scan of the piezo control voltages close to the optimum is also plotted. The irregular shape of the measured power is a result of a hysteresis effect when the horizontal control voltage was changed from its maximum value to the minimum.

6.4.2 The Mechanical Accelerometer

The periodic interferometer signal means that the interferometer phase is only proportional to acceleration over one fringe spacing $\Delta a = \frac{\pi}{k_{\text{eff}} T^2}$. Furthermore, the fringe spacing is inversely proportional to T^2 so there is a trade-off between dynamic range and sensitivity. These problems can be addressed by making use of a mechanical accelerometer mounted onto the back of the retro-reflecting mirror to form a hybrid system [20]. The accelerometer determines the acceleration up to the fringe spacing and the interferometer measures the acceleration more precisely. The accelerometer also measures the vibrations of the retro-reflecting mirror, so it can be used to filter the effects of vibration noise on the interferometer signal. This is discussed in more detail in Section 7.6.2. This hybridisation scheme has been used in measurements of gravity in high noise environments such as the centre of Paris [19] and in parabolic aircraft flights [12, 62].

The accelerometer is a navigation-grade AI-Q-2010 manufactured by *Innalabs*. This particular device was chosen because its specified intrinsic noise was $<7 \mu\text{g}$ in the 0-100 Hz bandwidth. For a pulse separation $T = 25 \text{ ms}$, the fringe spacing is $31.2 \mu\text{g}$ so it is sensitive enough to measure the acceleration to within one fringe. A schematic of this device is shown in Figure 6.9. It operates using a quartz pendulum which is free to move about one axis [63,64]. Under an acceleration, the deflection of the pendulum is capacitively detected. A servo loop circuit drives a current through the coils to restore the position of the pendulum. This current is directly proportional to the acceleration of the pendulum. This model has a nominal scale factor of $1.235\,976 \text{ mA g}^{-1}$. The acceleration is measured using a load resistance of $6 \text{ k}\Omega$ to give an output voltage of 7.56 V g^{-1} .

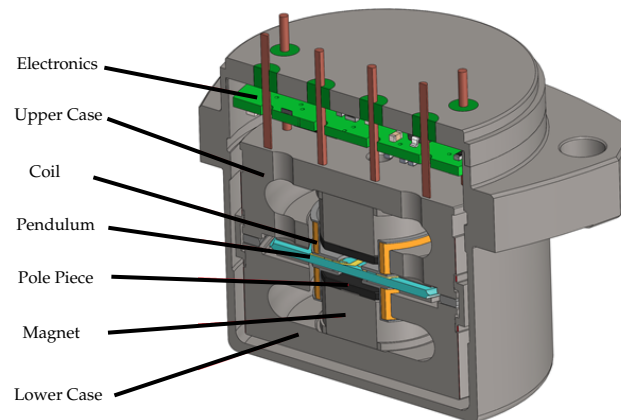


Figure 6.9: Cross-section of the Innalabs AI-Q-2010 accelerometer.

6.5 Conclusion

This chapter has motivated the need for low wavefront distortions to achieve sensitive measurements of acceleration, particularly when there is significant transverse motion across the Raman beam. Following this, the in-vacuum optical system was introduced. This helps to reduce the effect of wavefront distortions by not transmitting the beam

through an optical viewport. Finally, the retro-reflection assembly used to produce the counter-propagating beams has been presented.

